Journal of the Indian Society of Remote Sensing (2025) 53:2949–2964
https://doi.org/10.1007/s12524-025-02257-1

RESEARCH ARTICLE

Synergistic Use of EOS-06 Scatterometer and Doppler Weather Radar Observations for Coastal Wind Field Assessment: A Case Study

Vaibhav Tyagi[1] · Saurabh Das[1] · Bipasha Paul Shukla[2] · Abhisek Chakraborty[2] · Abhishek Chhari[2]

Received: 22 October 2024 / Accepted: 4 June 2025 / Published online: 5 July 2025

Abstract

The Oceansat-3 Ku-band Scatterometer (OSCAT-3) payload onboard the Earth Observation Satellite-06 (EOS-06), provides valuable global sea surface winds. The scatterometer was launched on November 26, 2022 by the Indian Space Research Organisation (ISRO). It is well known that the scatterometer measurements are contaminated in the presence of isolated rain events. The idea of the present study is to (i) study the impact of rain on OSCAT-3 wind retrievals in the presence of isolated rain events and (ii) explore the complementary role of Doppler Weather Radar (DWR) wind data in characterizing wind conditions near the coast during a pre-monsoon convection event. The study utilises OSCAT-3 observations from May 2024 collocated with ECMWF ERA5 and GPM-IMERG rain-rate over the Indian Summer Monsoon Region (ISMR). The statistical analysis reveals that the OSCAT-3 increasingly overestimate in low to moderate wind speed regime under increasing rain-rates. Furthermore, a case study of a pre-monsoon heavy rainfall event on May 18, 2024, revealed intense convection with INSAT-3D OLR values below 150 W/m^2 and high CAPE values reaching 3751.22 J/kg. DWR retrieved high-resolution 2D horizontal wind fields supplementing OSCAT-3 surface winds providing detailed insights into the precipitation system's dynamics. The DWR retrieved winds shows a significant convergence of the winds near the coast. The combined use of OSCAT-3 and DWR data enhances coastal wind analysis, providing a comprehensive understanding of wind field variations in the presence of heavy rainfall.

Keywords OSCAT-3 · EOS-06 · Doppler weather radar · Scatterometer winds · Heavy rainfall

Introduction

Sea surface winds are a crucial component in ocean–atmosphere interactions which serve as a primary driving force for upper ocean circulation and the interaction between surface winds and sea surface temperature (SST). Accurate measurements of surface winds over the oceans are an important factor for various meteorological and oceanographic applications (Sarkar, 2003). The scatterometer (radars onboard satellites) provide valuable sea surface winds by measuring the changes in backscatter over the ocean surface (Singh et al., 2022).

While the scatterometers provide valuable global wind field information, their measurements are affected by the presence of isolated rain events, affecting about 7% of the observations (Weissman et al., 2012). Numerous studies have been conducted to understand the impact of rain on scatterometer wind measurements. The scatterometer estimates the wind speed and direction based on the backscatter measurements and the presence of rain can affect the measurements in various ways: (i) raindrops, when hit the ocean surface, alters the ocean surface roughness which in turn changes the wind-induced backscatter; (ii) raindrops increase backscatter power due to the scattering of incident signals back to the sensor and (iii) raindrops also cause the extinction of signals because of absorption (Tournadre & Quilfen, 2003, 2005; Zhao et al., 2022; Weissman et al., 2012). Several studies have been conducted in the past to study and address these limitations. Studies suggest different approaches to addressing these issues: (i) Rain flagging

✉ Saurabh Das
das.saurabh01@gmail.com; Saurabh.das@iiti.ac.in

Vaibhav Tyagi
vaibhavtyagi7191@gmail.com

[1] Department of Astronomy, Astrophysics and Space Engineering, Indian Institute of Technology Indore, Indore, India

[2] Space Applications Centre (SAC), ISRO, Ahmedabad, India

method: this involves detecting the presence of rain and labelling the wind vector cell (WVC) as "rain affected". This flag information is provided with the scatterometer data for the user to either discard or use this observation with caution (Gohil et al., 2015; Huddleston & Stiles, 2000a, 2000b); (ii) Normalised radar cross section (NRCS) correction method, which involves correction of the NRCS considering the rain effects into model (Draper & Long, 2004; Hilburn et al., 2006; Weissman & Bourassa, 2008) and (iii) Empirical method, which involves estimating wind speed without considering the rain parameters (Stiles & Dunbar, 2010).

The information from the other sensors like ground-based and space-based can supplement the scatterometer observations. An attempt in this direction involved researchers using satellite-derived atmospheric motion vectors (AMV) with scatterometer observations to generate a merged wind field product for tropical cyclone analysis. Combining the satellite-based AMVs and scatterometer winds significantly increases the number of available wind vectors (Chakraborty et al., 2022; Nonaka et al., 2019). Similarly, the wind information from coastal DWRs plays an important role in providing additional wind field information in cases of isolated rainfall events where scatterometer measurements are ambiguous. The DWR provides 3D volumetric observation of radar reflectivity and radial velocity at very high spatial and temporal resolution over a limited area. In literature, various techniques have been proposed to retrieve the horizontal wind field from DWR radial velocity observations (Lhermitte, 1961; Li et al., 2015; Zhou et al., 2019). The radar-derived wind field offers the advantage of high spatial and temporal resolution. Additionally, it can also provide valuable wind information near the coast where scatterometer winds often become ambiguous due to potential land contamination (Owen & Long, 2009). Studies suggest that the convective development associated with extreme precipitation is significantly influenced by horizontal winds and their vertical structures (Chen et al., 2015; Pastushkov, 1975; Zhang & Atkinson, 1995). Therefore, DWR derived wind field plays an important role in understanding the physical mechanisms and dynamics of weather systems. A study by Priftis et al. (2018) utilised ground-based Next Generation Doppler weather radar (NEXRAD) in conjunction with Advanced Scatterometer (ASCAT) observations to examine the wind characteristics of oceanic mesoscale systems. The study reveals that the wind field retrieved from NEXRAD provided valuable and accurate near-surface winds in cases of heavy precipitation where the ASCAT wind speed and direction were ambiguous.

Several researchers have evaluated the quality of the surface winds from previous scatterometer missions and found a good correlation, in general against the ground truth highlighting the reliability of the scatterometer data. Chacko and Jayaram (2024) analysed the quality of wind products from the recently launched OSCAT-3 scatterometer and found a good agreement between the OSCAT-3 winds and observations from moored buoys and ASCAT. However, the performance of OSCAT-3 wind products under rainy conditions is yet to be understood. Therefore, the present study first aims to analyse the performance of OSCAT-3 scatterometer winds under rainy conditions over the Indian Summer Monsoon Region (ISMR). The study utilizes the OSCAT-3 wind observations from May 2024. Next, the study demonstrates the potential of combining DWR and OSCAT-3 winds for a detailed understanding of coastal precipitating systems. A case study utilizing simultaneous OSCAT-3 and DWR winds during a pre-monsoon heavy rainfall event that occurred on May 18, 2024, over the southern peninsula is analysed for this purpose. The domain of ISRO's Thumba Equatorial Rocket Launching Station (TERLS) DWR (as shown in Fig. 1) is considered for feasibility and demonstration of the concept. This site is also vital as an entry point to the propagation of the Southwest monsoon to the Indian landmass.

The paper is organized as follows: Section "Data and Methods" provides an overview of the dataset and methodology used in the study. Subsequently, the impact of rain on OSCAT-3 wind observations and a case of a pre-monsoon heavy rainfall event utilizing simultaneous OSCAT-3 and TERLS DWR wind information is presented in the Section "Results and Discussion". The summary and the key conclusions are presented in the Section "Summary and Conclusion".

Data and Methods

Datasets

OSCAT-3 Wind Data

The study utilizes data from an active Ku-band (13.5156 GHz) scatterometer. The OSCAT-3 payload onboard the EOS-06 launched by the Indian Space Research Organisation (ISRO) on November 26, 2022 from Satish Dhawan Space Centre (SDSC). Continuing the legacy of its predecessor, SCATSAT-1, it provides global 2D wind field information. The technical specifications of the OSCAT-3 payload are described in Table 1. Operational products are generated and disseminated at various levels, including L1B (scan mode sigma-0), L2A (grid mode sigma-0), L2B (grid mode wind), L3SH(V) (global sigma-0 H(V) polarization), and L3W (global wind product), along with various scientific products. These products are made available to the user community via

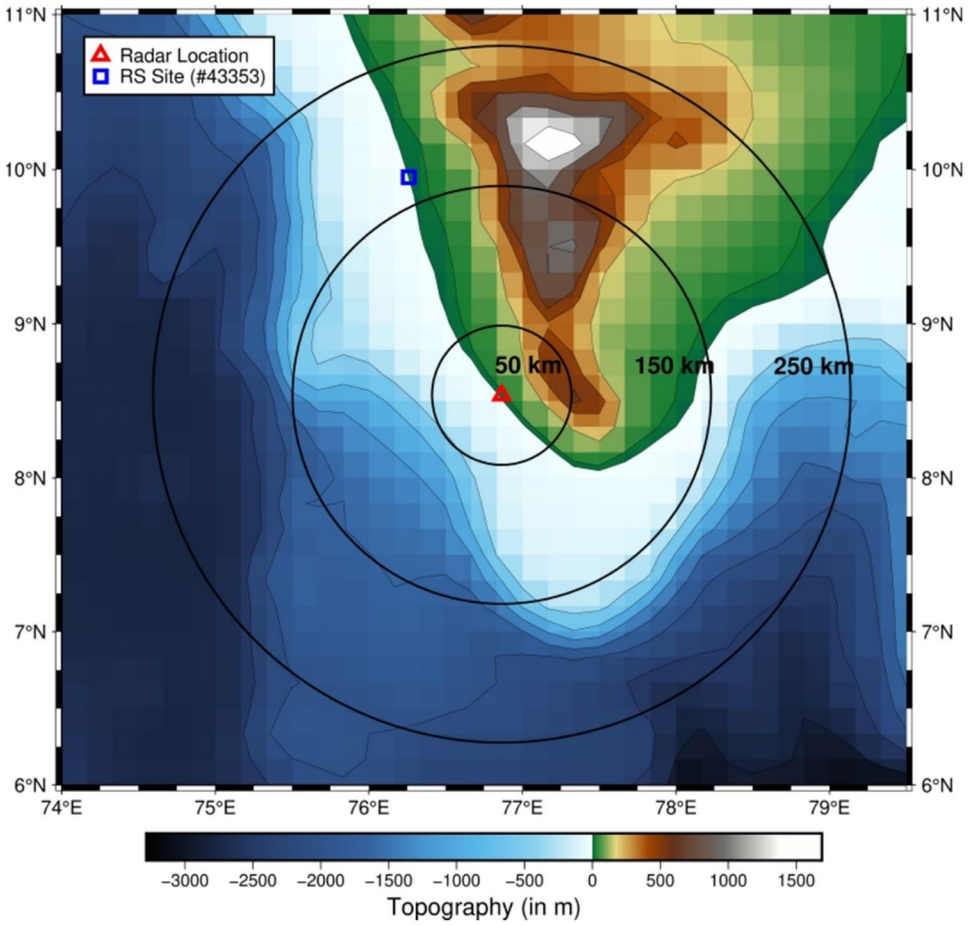

Fig. 1 Topographic map of the study region. The red triangle represents the TERLS DWR site, while the blue square represents the Cochin radiosonde site. Concentric rings at distances of 50, 150, and 250 km are shown, centred at the radar location (Color figure online)

the Bhoonidhi (https://bhoonidhi.nrsc.gov.in/bhoonidhi) portal of the National Remote Sensing Centre (NRSC).

The L2B (Level 2) swath mode wind product available in Hierarchical Data Format (HDF5) was used in the present study. This product is available at spatial resolutions of both 12.5 km and 25 km with the high-resolution 12.5 km product being utilized to better resolve near-surface wind features. The product also includes rain flag information stored as a 16-bit unsigned integer, which is used to study the effect of rain. A Quality Flag (QF) value of 1 denotes quality-controlled vectors, while a QF value of 3 indicates rain-flagged vectors. Additionally, the rain-corrected wind speed is also provided in the OSCAT-3 L2B product. The rain-corrected wind speed provided in the OSCAT-3 L2B product are estimated based on a Bayesian estimation technique proposed by Gopalan et al. (2019). The performance evaluation of the technique shows a significant reduction in wind speed bias and root mean wind speed. The study also utilises the OSCAT-3 L4 product of daily analysed OSCAT-3 winds to study the wind divergence, obtained from the Meteorological and Oceanographic Satellite Data Archival Centre (MOSDAC, https://www.mosdac.gov.in).

Table 1 Technical specifications of OSCAT-3 payload

Parameter	Remark
Satellite Altitude	734–767 km
Orbit	Polar, Sun Synchronous
Inclination	98°
Frequency	13.5156 GHz
Antenna Diameter	1.4 m
Polarization	HH for Inner and VV for Outer beams
Swath	1400 km (both HH and VV beams)
	1400–1800 km (only VV beam)
Wind Vector Cell Size	25 km × 25 km & 12.5 km × 12.5 km
Wind Speed Range	3–30 m/s
Wind Speed Accuracy	25 km × 25 km: ~ 1.6 m/s rms or 10% whichever is higher
	12.5 km × 12.5 km: ~ 1.8 m/s rms or 10% whichever is higher
Wind Direction Range	0° to 360°
Wind Direction Accuracy	20° rms

The values quoted here are adopted from EOS-06 coffee table book, (CTB-EOS-06, 2023)

ECMWF Reanalysis Data

The surface winds from the European Centre for Medium-Range Weather Forecasts (ECMWF) Reanalysis v5 (ERA5) are used to evaluate OSCAT-3 surface winds. The ECMWF ERA5 provides long-term global reanalysis data using numerical models and data assimilation techniques. The ERA5 reanalysis data is available as a global 0.25° × 0.25° gridded product with a 1-h temporal resolution. A comparison of ERA5 and ERA-Interim with ASCAT indicates that ECMWF ERA5 generally performs better than ERA-Interim in representing surface winds (Belmonte & Stoffelen, 2019). Hence, ERA5 is used in this study obtained from the Copernicus Climate Data Store (https://cds.climate.copernicus.eu).

GPM-IMERG Rainfall Data

The present study utilizes the Integrated Multi-Satellite Retrievals for Global Precipitation Measurement (GPM) (IMERG) Final Run V07 product (Huffman et al., 2015) which provides high-resolution gridded rainfall data at a temporal resolution of 30 min and a spatial resolution of 10 km. The GPM-IMERG rainfall data is obtained from NASA's Earthdata portal (https://search.earthdata.nasa.gov). The GPM-IMERG estimates global precipitation measurements using the GPM constellation satellites. Saikrishna et al. (2021) evaluated the performance of various satellite-based precipitation products over the Indian region and found that the GPM Final Run shows good agreement with the India Meteorological Department (IMD) gridded rainfall product.

Doppler Weather Radar Data

The present study utilizes the TERLS C-band dual-polarized DWR observations obtained from MOSDAC (https://www.mosdac.gov.in). The TERLS DWR installed at Thiruvananthapuram in Kerala (Latitude: 8.53° N and Longitude: 76.86° E). The location of the radar with the topography is shown in Fig. 1. The specifications of TERLS DWR are provided in Table 2 and more details on the radar system can be found in Mishra et al. (2020). The study utilizes the L2B (Level 2) product in dual pulse repetition frequency (DPRF) mode which includes base and dual-polarized variables such as reflectivity (Z), radial velocity (Vr), spectral width (σ), differential reflectivity (Zdr), differential propagation phase (Φdp), and cross-correlation coefficient (ρhv). These variables are available in Plan Position Indicator (PPI) scan mode at 11 different elevation angles: 0.5°, 1°, 2°, 3°, 4°, 7°, 9°, 12°, 15°, 18°, and 21°.

Auxiliary Data

The present study utilizes daily outgoing longwave radiation (OLR) estimates derived from the Indian National Satellite-3D (INSAT-3D) imager which are obtained from MOSDAC (https://www.mosdac.gov.in). The OLR values are estimated using narrow-band radiances from the WV, TIR-1, and TIR-2 channels providing information of atmospheric energy fluxes. The OLR data is used to study the potential of convective activity over the region. To analyze the atmospheric and synoptic conditions, the study utilizes the radiosonde observations from the University of Wyoming (https://weather.uwyo.edu/upperair/sounding.html). Since radiosonde observations for Thiruvananthapuram were unavailable, data from the nearest station Cochin (9.95° N, 76.26° E) was used. Radiosonde data is further utilized to construct a Skew-T log-P diagram to analyse the vertical profile of the atmosphere providing insights into atmospheric stability, moisture distribution and the potential for convective activity.

Methodology

A detailed flowchart representation of the methodology adopted is shown in Fig. 2.

OSCAT-3 Data Pre-processing

The 12.5 km L2B swath wind product is obtained from NRSC's Bhoonidhi portal consists of 1720 rows and 144 cells. It is subsetted to extract the data over the area of interest. The extracted data includes a list of wind vector cells (WVC) with information on latitude, longitude, wind speed (WS), wind direction (WD) and quality flag (QF). The wind speed and direction are used to estimate the horizontal wind field components: zonal wind component (U) and meridional wind component (V) at 10 m height using Eqs. (1) and (2). (Note that a factor of 90 is considered to account for the bias in direction between geometrical and oceanographic convention.)

Table 2 Specifications of TERLS Doppler Weather Radar

Properties	TERLS DWR
Frequency	5.6–5.65 GHz (C band)
Polarization	Dual
Latitude	8.5374° N
Longitude	76.8657 ° E
Altitude	27 m
Range resolution dprf* (sprf)	150 m (300 m)
Maximum range dprf (sprf)	240 m (364.8 m)
No. of elevation angles dprf (sprf)	11 (3)

*dprf (sprf) stands for dual (single) pulse repetition frequency mode

$$U = WS * Cos(90 - WD) \quad (1)$$

$$V = WS * Sin(90 - WD) \quad (2)$$

Collocation of OSCAT-3, ECMWF ERA5 and GPM-IMERG Observations

In order to study the effect of rain on OSCAT-3 surface wind observations we prepared a collocated dataset of OSCAT-3, ECMWF ERA5 and GPM-IMERG observations by performing spatio-temporal matching. The spatial and temporal resolution of the three datasets is different. The OSCAT-3 observations are available as swath data at 12.5 km spatial resolution while the data from ECMWF ERA5 and GPM-IMERG is gridded data at 25 km and 10 km respectively. The data from ECMWF ERA5 and GPM-IMERG is available at every 1 h and 30 min respectively. The k-d tree algorithm was used to find the nearest neighbour for OSCAT-3 observations considering a temporal tolerance of 25 min and spatial as 8 km.

To evaluate the performance of OSCAT-3 wind speed measurements various statistical metrics like root mean square error (RMSE), bias (Bias) and correlation coefficient (r) are calculated using Eq. (3–5).

$$Bias = \frac{1}{N}\sum_{i=1}^{N}(E_i - O_i) \quad (3)$$

$$\mathrm{RMSE} = \sqrt{\frac{1}{N}\sum_{i=1}^{N}\left(E_i - O_i\right)^2} \quad (4)$$

$$r = \frac{\sum_{i=1}^{N}(E_i - \overline{E})(O_i - \overline{O})}{\sqrt{\sum_{i=1}^{N}\left(E_i - \overline{E}\right)^2\left(O_i - \overline{O}\right)^2}} \quad (5)$$

where N is the number of collocated observations and E (O) for ECMWF ERA5 (OSCAT) observations.

Quality Control of DWR Observations

DWR provides the return signal from the meteorological targets, however, in some cases, the signal is contaminated by the return from non-meteorological targets commonly known as clutter. As shown in Fig. 1, to the 40–50 km north-east of the radar, the presence of Western Ghats results in significant beam blockage at lower elevations. Panda (2019) reported that there the north-eastern sector of the radar

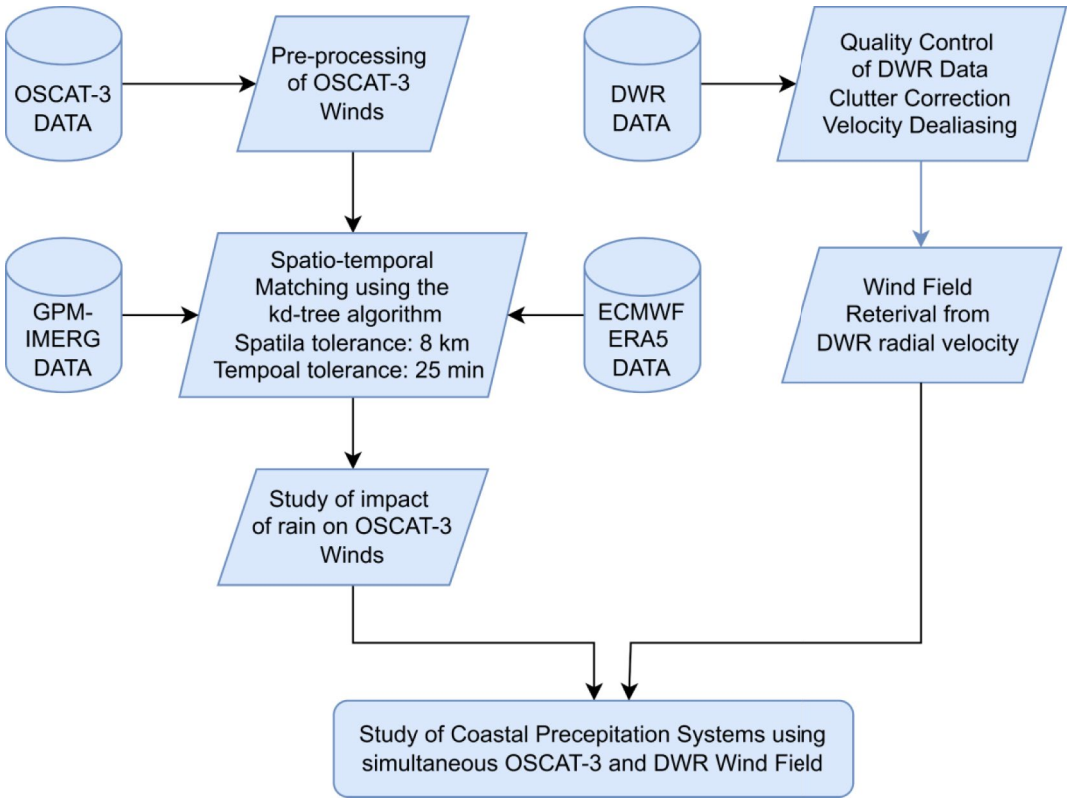

Fig. 2 Flowchart representation of the methodology adopted

experience significant blockage with beam blockage fraction reaching close to 1. Apart from this, the presence of hills also contaminates the radar reflectivity observation and requires appropriate postprocessing techniques to mitigate these effects.

Quality control in the context of DWR observations is an important step to ensure the accuracy and reliability of radar observations. The present study utilizes polarimetric observations like reflectivity (Z), radial velocity (V_r), differential reflectivity (Z_{dr}), differential propagation phase (Φ_{dp}) and cross-correlation (ρ_{hv}) for clutter removal to enhance the quality of radar observations. It considers clutter information using Gabella and Notarpietro (2002) to identify and mask clutter regions and processes it using fuzzy logic by assigning weights to each variable using Vulpiani et al. (2012). Furthermore, if the velocity exceeds a maximum unambiguous velocity called Nyquist velocity, the radial velocity measured by the radar is underestimated and folded over. This is commonly known as velocity aliasing. The study employed an automated 2D multipass velocity dealiasing approach, focusing on maintaining the horizontal continuity of velocity fields by identifying reference radials and gates within the low wind shear regions Zhang and Wang (2006). The major advantage of this technique is that it doesn't require any external reference velocity data, enhancing its applicability. The quality controlled radial velocity observation is used further to retrieve the horizontal wind field.

Wind field retrieval from DWR observations

The DWR measures the radial component of velocity, which can be used to retrieve the local wind field through a linear wind field model. A commonly utilized technique for retrieving wind profiles from single-Doppler radar data is the Velocity Azimuth Display (VAD). This approach involves fitting a sinusoidal curve through data sets to determine radial mean Doppler velocity (Browning & Wexler, 1968; Lhermitte, 1961). However, the VAD technique estimates the horizontal wind profiles just above the radar site. To better understand the system's dynamics, it necessitates retrieving a 2D horizontal wind field from single-Doppler radar data. We employ a 2D horizontal wind field retrieval algorithm (known as SingleDop) based on Xu et al. (2006). The algorithm utilizes VAD to generate a background wind field and corrects it using raw radial velocity observations accounting for error covariance. Based on the estimation of the 2D cross-covariance function between the radar's radial and tangential wind components, the technique retrieves an accurate low-level 2D wind field along a conical surface.

Results and Discussion

The scatterometer provides valuable global sea surface wind information; however, a known limitation, as already mentioned, is the contamination of wind retrievals in the presence of isolated rain events. Several studies in the past explored this aspect for different scatterometer missions. In order to understand this effect on the newly launched EOS-06 OSCAT-3 scatterometer, an example of the OSCAT-3 wind speed on May 19, 2024 at 19:00 UTC is shown in Fig. 3a. The corresponding rain-rate from GPM-IMERG and ECMWF-ERA5 wind speed is shown in Fig. 3b and c respectively. It can be seen that there is a significant variation between OSCAT-3 and ECMWF ERA5 wind speed in regions with enhanced rain-rate. These necessities the understanding of how OSCAT-3 observations are affected by rain under different rain-rate regimes. The following section presents a statistical analysis of the impact of rain on OSCAT-3 observations.

Statistical Analysis of the Impact of Rain on OSCAT-3 Observations

The analysis is performed over the Indian Summer Monsoon Region (ISMR) covering the latitude range 10° S to 25° N and longitude range 40° to 120° E. OSCAT-3 observations of one month (May 2024) is considered for the statistical analysis. The collocation of OSCAT-3, GPM-IMERG, and ECMWF-ERA5 data is performed as outlined in the methodology. A total of 1,425,359 collocated observations are found. The 2D histogram of collocated OSCAT-3 and ECMWF-ERA5 wind speed and wind direction is shown in Fig. 4. There exists an overall good agreement between both datasets with correlation coefficients of 0.74 and 0.81 for wind speed and wind direction, respectively. The RMSE value for wind speed is 2.19 m/s and that of wind direction is 73.07°.

Figure 5 shows the 2D histogram for OSCAT-3 and ECMWF-ERA5 wind speed and direction for different rain-rate conditions. The rain-rate (R) conditions considered are $R = 0$, $0 < R < 1$, $1 \leq R < 3$, $3 \leq R < 5$ and $R \geq 5$. The number of collocated samples and the statistical metrics are given in Table 3. The impact of rain-rate on OSCAT-3 winds is evident from the different metrics in Table 3. As the rain-rate increases, the correlation coefficient decreases whereas the RMSE and mean bias increases. It is observed that the OSCAT-3 wind speed tends to overestimate more in the low wind speeds than at higher wind speeds under increasing rain-rates (Fig. 5). The effect is more prominent at higher rain rates. This is due to the fact that rain enhances the backscatter and these effects dominate at low to medium wind speeds (Stiles & Yueh, 2002). This highlights that OSCAT-3

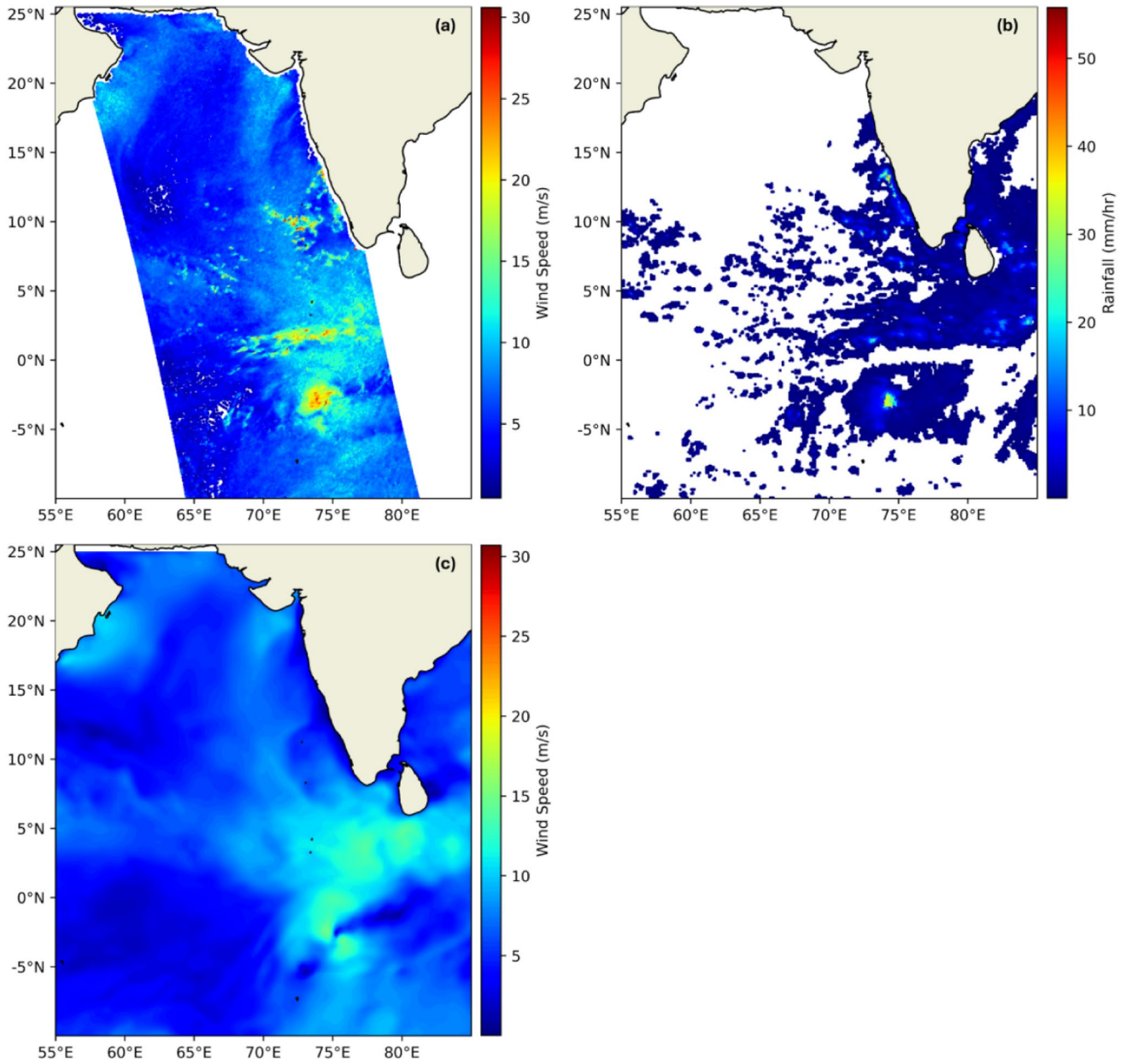

Fig. 3 **a** An example of the OSCAT-3 wind speed over the Indian Summer Monsoon Region on May 19, 2024 at 19:00 UTC **b** spatial distribution of rainfall from GPM-IMERG for the nearest time corresponding to (**a**), and **c** wind speed from ECMWF ERA5 reanalysis data at surface level

winds tend to be overestimated in the low to medium wind speed range and may be used considering these effects.

Case Study

A case study of a pre-monsoon heavy rainfall event occurred on May 18, 2024 over the southern peninsular region is presented in this section. The event started around 12:00 UTC of May 18 till 14:00 UTC of May 19, 2024. As per IMD, a low and mid-tropospheric-level cyclonic circulation was developed over the south interior of Tamil Nadu and its neighbourhoods. This results in widespread rainfall accompanied by thunderstorms and lightning activity over the southern peninsula region (IMD-Press Release, 18 May, 2024).

Overview of Synoptic Conditions

This section briefly describes the synoptic condition to understand the background dynamics favourable to the heavy

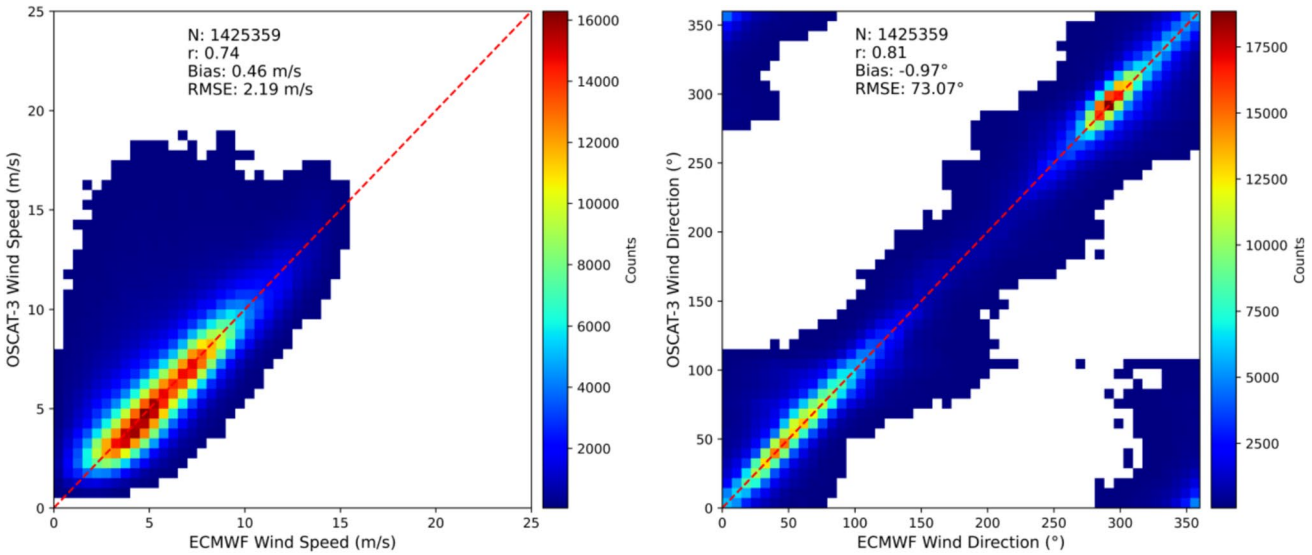

Fig. 4 **a** 2D histograms of collocated wind speed of OSCAT-3 surface winds and ECMWF ERA5 surface winds. **b** same as (**a**) but for wind direction. Red dashed line shows 1:1 line (Color figure online)

rainfall event that occurred on May 18, 2024 started around 12:00 UTC. We analysed daily outgoing longwave radiation (OLR) derived from INSAT-3D to identify the intensity of convection on the event day as shown in Fig. 6a. OLR values below 200 W/m2 are indicative of deep convection in the tropical region (Fu et al., 1990; Xavier et al., 2018; Zhang, 1993). Figure 6a shows the OLR values of less than 150 W/m^2 to the west of the southern peninsula tip. Such low values of OLR correspond to lower cloud top temperatures, indicating higher cloud tops and thus signifying strong convection. According to Xavier et al. (2018) the moist convective instability and a notably higher amount of convective available potential energy (CAPE) are the characteristics of a tropical monsoon environment. The sounding observations for the Cochin station (9.95° N and 76.26° E) are used to estimate the CAPE during the event. The SkewT-Log P plot at 00Z on May 18, 2024, over Cochin (Fig. 6b) illustrates an unstable atmosphere characterized by significantly high CAPE values, reaching 3751.22 J/kg, suggesting enough energy is available to drive convection. Subrahmanyam and Kumar (2022) also reported a similar surge in CAPE values prior to the extreme rainfall event of the 2018 Kerala floods. The convective inhibition (CIN) is notably low at -9.04 J/kg, signifying that only a small amount of energy is required to lift an air parcel to its level of free convection (LFC). The LFC is at about 908 hPa, and the lifting condensation level (LCL) is at about 947 hPa, which is very close to the surface, implying that air parcels ascending from the surface will promptly condense and form clouds. The dewpoint temperature (green curve) is close to the temperature (red curve) till 500 hPa, which indicates high relative humidity due to the influx of moist air from the Arabian Sea. This suggests a favourable environment for intense convection activity. Figure 7 shows the daily accumulated precipitation from GPM IMERG on May 18, 2024, with accumulated precipitation exceeded 350 mm to the south of the radar.

Combined DWR and OSCAT-3 Wind Field Analysis

Figure 8 shows the PPI plot of TERLS DWR radar reflectivity at a 2-degree elevation angle highlighting the spatiotemporal evolution of the precipitating system. The analysis spans from 17:52 UTC to 21:34 UTC on May 18, 2024. The PPI time series indicates the presence of a precipitation system within the radar's 150 km coverage area. It shows that the system originated over the Arabian Sea and progressed towards the coastal region in the south-east direction. At 17:52 UTC radar reflectivity reveals various convective systems with high reflectivity values reaching up to 40 dBZ. Notably, a linear structure in reflectivity forming an organised precipitation band can be observed at 20:18 UTC to the southeast of the radar.

As described in the methods section, the radial velocity measured by the radar can be used to retrieve the horizontal wind field. The radar radial velocity observations are available at very high resolution, with a 150 m range resolution and 1-degree azimuth. This enables the generation of high-resolution 2D horizontal wind field up to 1 km spatial resolution over a conical surface. A typical scan strategy for TERLS radar is shown in Fig. 9. The different elevations are shown in different colors, with a solid dashed line representing the beam centre, and the 3 dB beam width shown by the shaded region. It can be seen that the beam heights increase as the distance from the radar increases, reaching

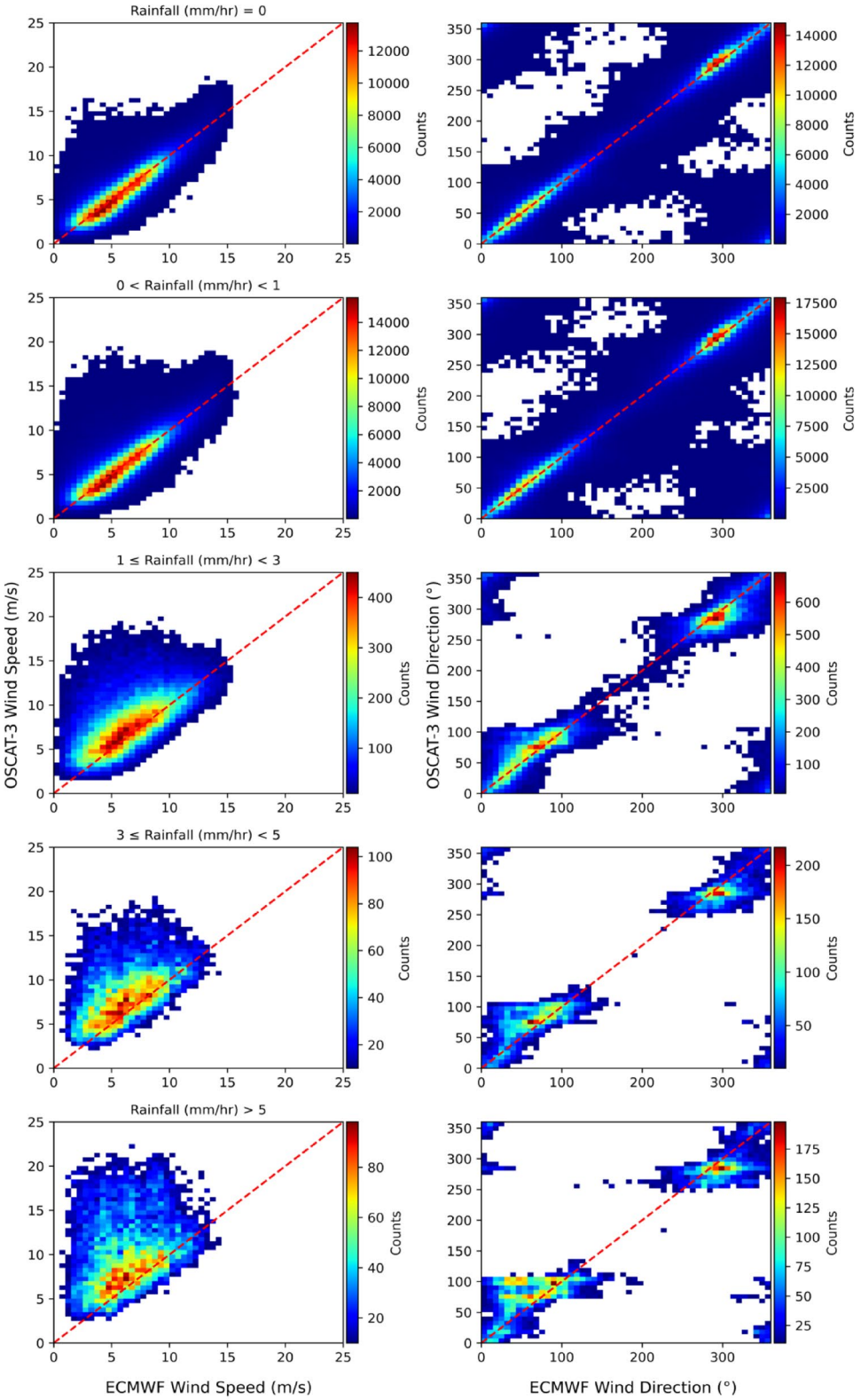

Fig. 5. 2D histograms of OSCAT-3 and ECMWF ERA5 surface winds collocated observations for May 2024 for different rain rates. Left columns is for wind speed and right for wind direction. Red dashed line shows 1:1 line (Color figure online)

Table 3 Statistical metrics for OSCAT-3 and ECMWF ERA5 wind speed and wind direction comparison with different rain rates

Rain rate (mm/hr)	N (Number of Collocations)	Wind Speed			Wind Direction		
		Correlation coefficient, r	Bias (m/s)	RMSE (m/s)	Correlation coefficient, r	Bias (°)	RMSE (°)
R = 0	977,511	0.85	0.09	1.44	0.83	− 1.33	70.99
0 < R < 1	261,202	0.7	0.91	2.5	0.81	− 0.57	74.26
1 ≤ R < 3	74,968	0.49	2.03	3.94	0.76	1.41	82.89
3 ≤ R < 5	21,510	0.36	3.32	5.43	0.7	2.38	91.25
R > 5	24,464	0.25	4.9	7.19	0.69	2.75	92.03

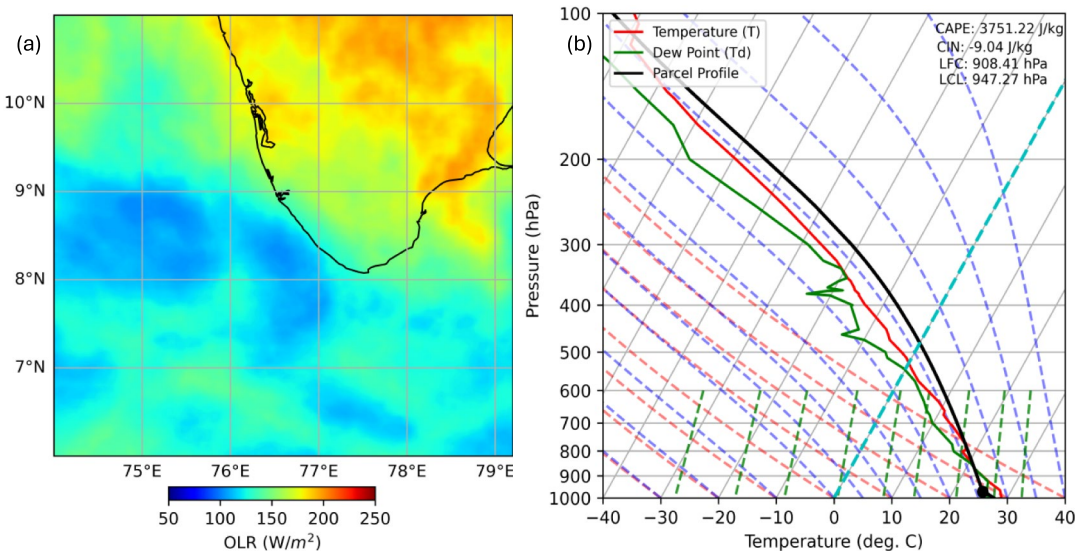

Fig. 6 **a** Daily INSAT-3D derived OLR for May 18, 2024. **b** The SkewT-Log P sounding plot for Cochin station for May 18, 2024, at 00 UTC. Values for various parameters, including CAPE, CIN, LFC, and LCL, are indicated in the top right

up to a height of ~2 km at a distance of 125 km. Thus, the radar observations shown are not at constant altitude but are projected on the 2D plane. Figure 10 shows the time series of a 2D horizontal wind field at a 2-degree elevation, corresponding to the radar observations as shown in Fig. 8. The wind vectors are downscaled to enhance visibility. These radar-derived 2D horizontal wind fields can be used to supplement the wind information as measured by the scatterometer in cases of heavy precipitation. The OSCAT-3 ascending pass (SN) on May 18, 2024, at 18:24 UTC is shown in Fig. 11, with the GPM-IMERG rain rate shown as a contour in the background. High rain rates reaching up to 20 mm/hr were observed (Fig. 11), corresponding to the precipitation system with high reflectivity values as shown in Fig. 8. These can significantly affect the scatterometer wind speed, as revealed by the red rain-flagged vectors as shown in Fig. 11.

Figure 12a shows the OSCAT-3 wind fields (black and red vectors) and DWR-retrieved wind fields (blue vectors) at 2-degree elevation. The scatterometer winds provide information about near-surface winds at the 10-meter level, while radar-retrieved 2D horizontal winds are estimated on a conical surface projected on a 2D plane. The scatterometer shows the surface winds of about 10 m/s flowing towards the Indian landmass. While the scatterometer captures the surface wind conditions, the DWR-retrieved 2D horizontal winds provide valuable insights into precipitation dynamics. The DWR-retrieved 2D horizontal winds demonstrate notable wind convergence over a wider region, as illustrated in Fig. 12a. It is important to note that the DWR-retrieved 2D horizontal winds are at 1 km spatial resolution. Due to the limited resolution, no such convergence of wind field is observed in ERA5 winds at 850 hPa, as shown in Fig. 13a and b. The observed agreement in wind direction and the enhanced convergence near the coast seen in both DWR and OSCAT-3 L4 products (Fig. 14) indicate a localized uplift mechanism. This likely contributed to the formation of precipitating clouds, resulting in the heavy rainfall on May 18, 2024.

The 3D plot of radar derived wind speed (with 4 lowest sweeps) along with the scatterometer winds as a base layer is shown in Fig. 12b. Wind barbs from the nearest

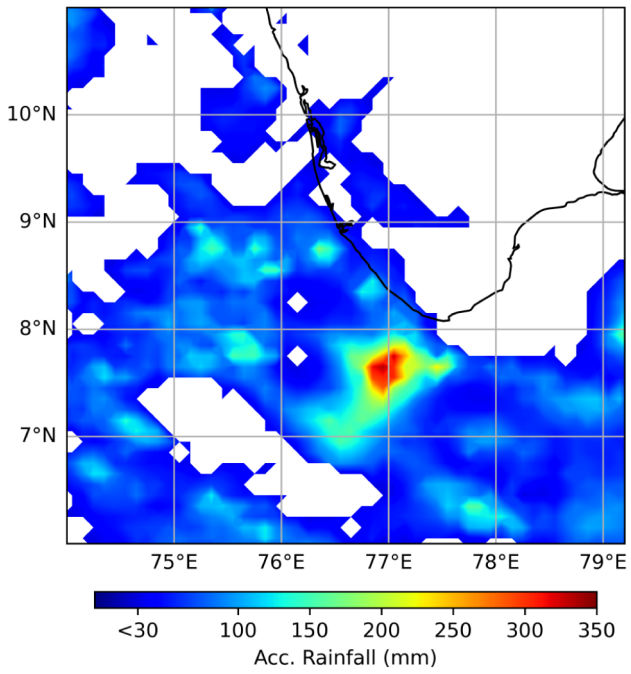

Fig. 7 The GPM-IMERG daily accumulated rainfall (in mm) on May 18, 2024

available sounding are also shown with barbs in red. Previous studies suggest that radar-derived wind field at low elevations are reliable to study near-surface wind features (Priftis et al., 2018).

The integration of wind data from DWR and spaceborne scatterometers like OSCAT-3 offers a complementary view of atmospheric dynamics, particularly beneficial for high-impact weather systems. OSCAT-3 provides global surface wind data every two days which limits its ability to capture rapidly evolving weather events. In coastal regions, this limitation can be addressed by complementing OSCAT-3 data with high-resolution wind information from DWR. Each sensor provides a unique perspective, and their fusion can bridge observational gaps, enhance analysis, and improve predictive capabilities such as: complementary coverage and resolution, enhanced monitoring and tracking of extreme weather events (e.g., tropical cyclones), improved nowcasting etc. These features of the combined winds not only add to the available quality observations but also help in giving better insights of meso-scale phenomena like precipitation dynamics through improved low-level winds etc. In a nutshell, the combined wind data can substantially improve our

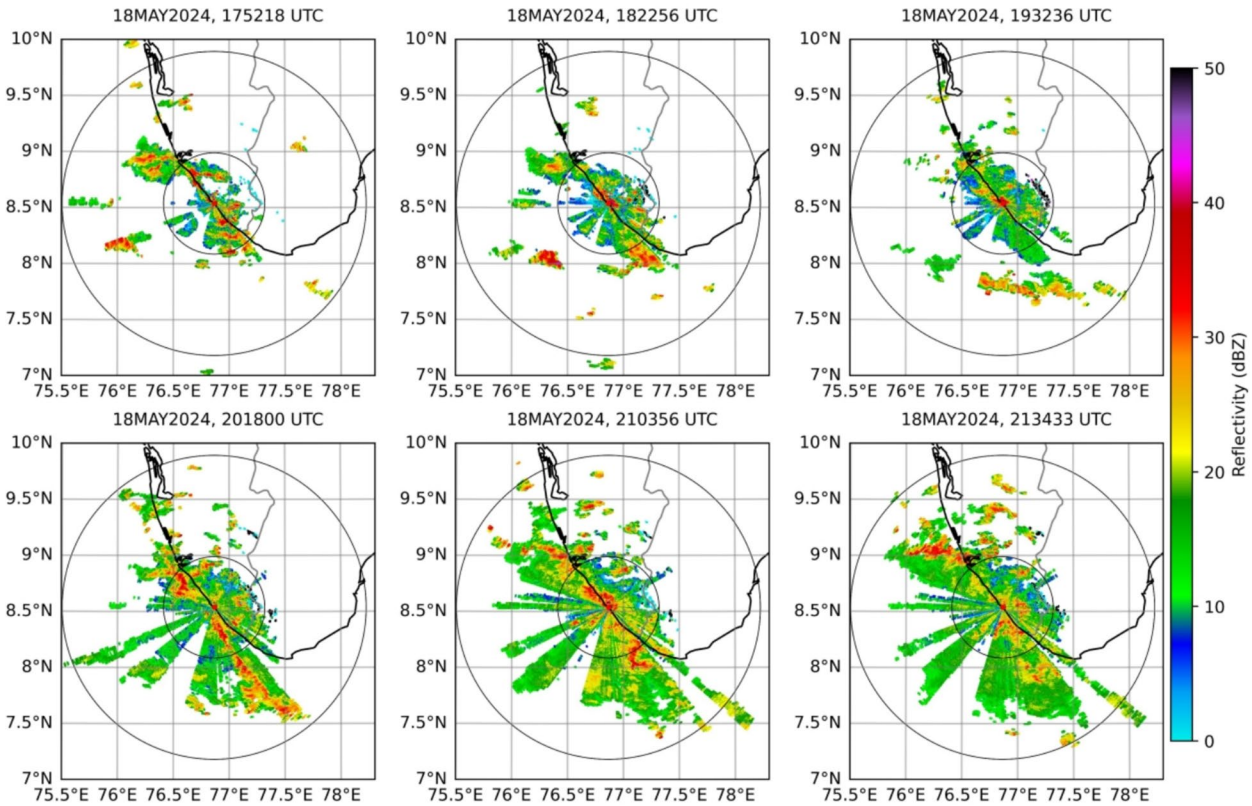

Fig. 8 PPI time-series of DWR reflectivity from 17:52:18 UTC to 21:34:33 UTC on May 18, 2024, at 2° elevation. Concentric rings at distances of 50 and 150 km are shown, centred at the radar location

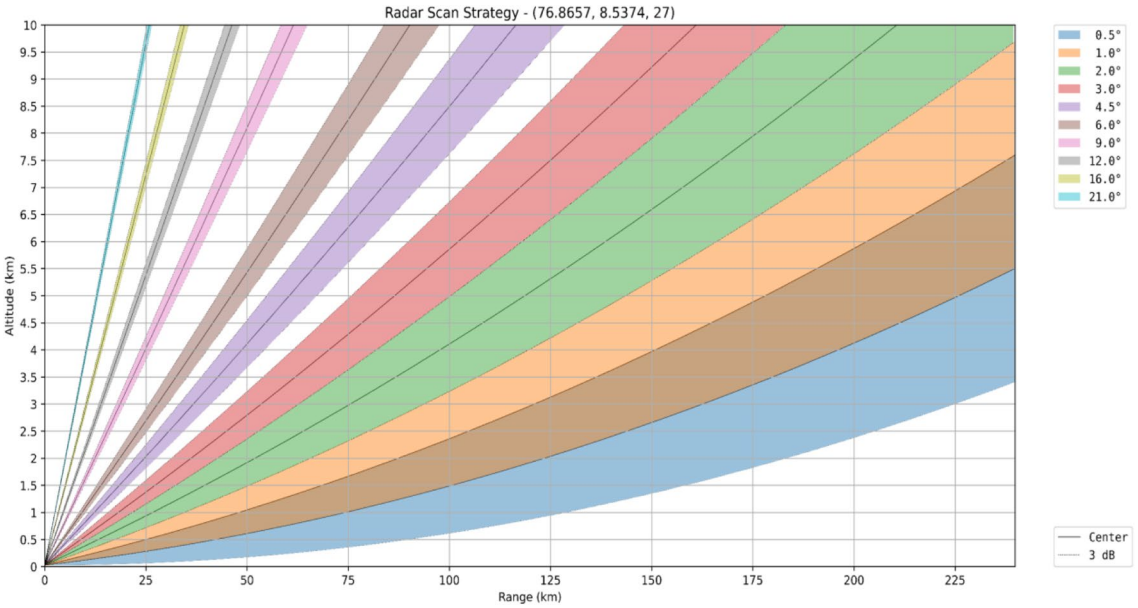

Fig. 9 Radar scan strategy for TERLS DWR illustrating radar beam height variation with elevation angles, represented by different colors. The dotted lines indicate the beam centre, while the shaded regions depict the 3 dB beamwidth

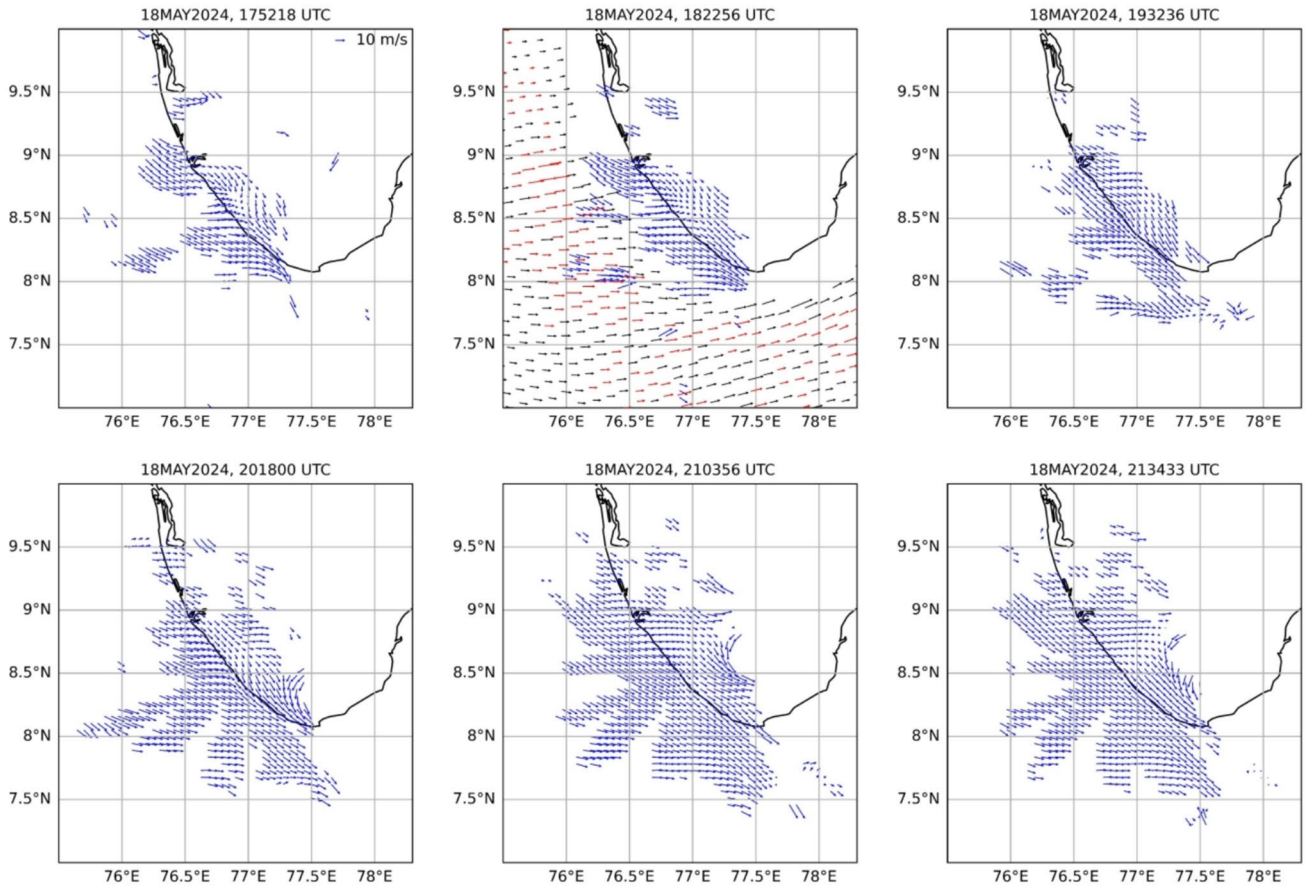

Fig. 10 Time-series of DWR retrieved horizontal wind field from 17:52:18 UTC to 21:34:33 UTC on May 18, 2024, at 2° elevation. OSCAT-3 winds at 18:24 UTC closest to DWR retrieved winds at 18:22 UTC are shown in background. A reference for wind vector length is provided at the top left for a wind speed of 10 m/s

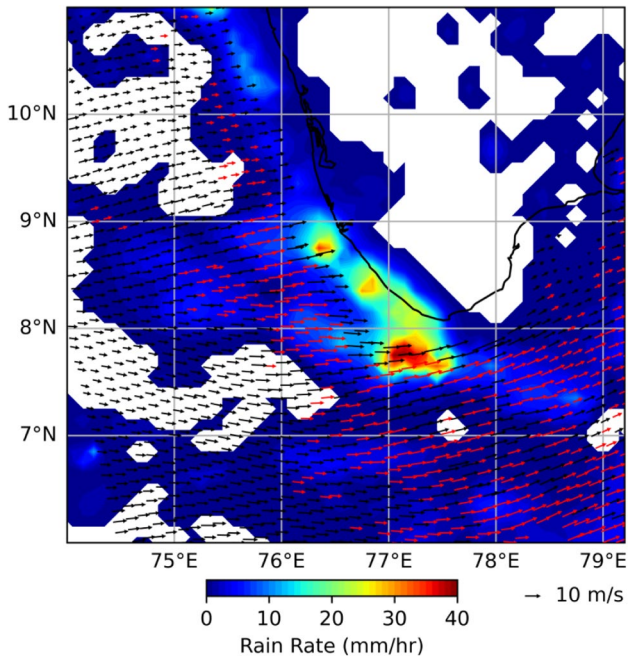

Fig. 11 The OSCAT-3 swath of wind vectors of the ascending node (SN) at 12.5 km on May 18, 2024, at 18:24 UTC, corresponding to the radar coverage area. Here black vectors represent best quality vectors and red vectors denote rain-flagged vectors. The background depicts the GPM-IMERG rain-rate. A reference for wind vector length is provided at the top left for a wind speed of 10 m/s. (Color figure online)

understanding of atmospheric phenomena by providing a multi-dimensional, multi-scale wind field that supports both scientific analysis and operational forecasting. This synergy enhances early warning capabilities, model performance, and decision-making in weather-sensitive sectors. Future work would focus on merging the two datasets to enhance the accuracy and reliability of coastal wind analysis, which is crucial for improving weather prediction and climate modeling.

It is also to be noted here that the combined wind filed analysis is restricted by the limited spatial overlap between OSCAT-3 and DWR derived winds. Also, the present study uses the SingleDop wind retrieval technique based on Xu et al. (2006) which provides the accurate near surface wind features on conical surface. Finally, the study highlights the benefits of using DWR to complement the scatterometers lower temporal resolution, especially in rapidly evolving weather systems. However, the case study focuses on a single event, and further studies over multiple events are necessary to generalize the findings and fully assess the potential of using simultaneous DWR and OSCAT-3 for coastal wind field analysis in diverse weather conditions.

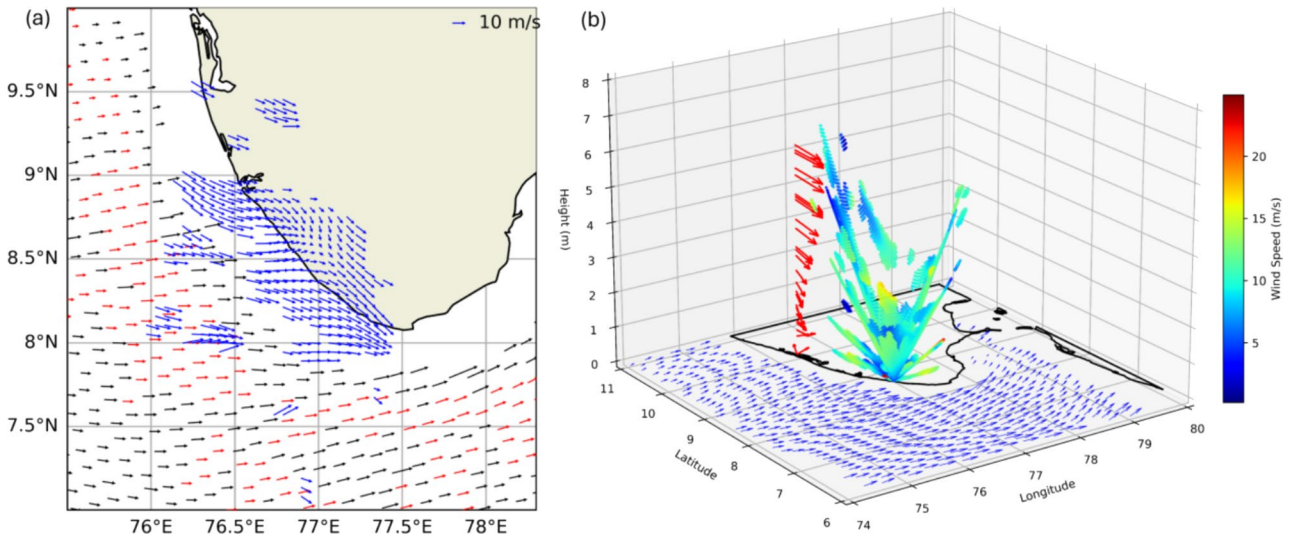

Fig. 12 **a** The OSCAT-3 wind vectors at 12.5 km on May 18, 2024, at 18:24 UTC, corresponding to the radar coverage area along with DWR retrieved horizontal winds at 18:22 UTC in blue. A reference for wind vector length is provided at the top left for a wind speed of 10 m/s. Here black vectors represent best quality vectors, and red vectors denote rain-flagged vectors. **b** 3D wind speed from DWR (with 4 lowest sweeps) with base layer as scatterometer winds (in blue) and radiosonde wind barbs (in red) (Color figure online)

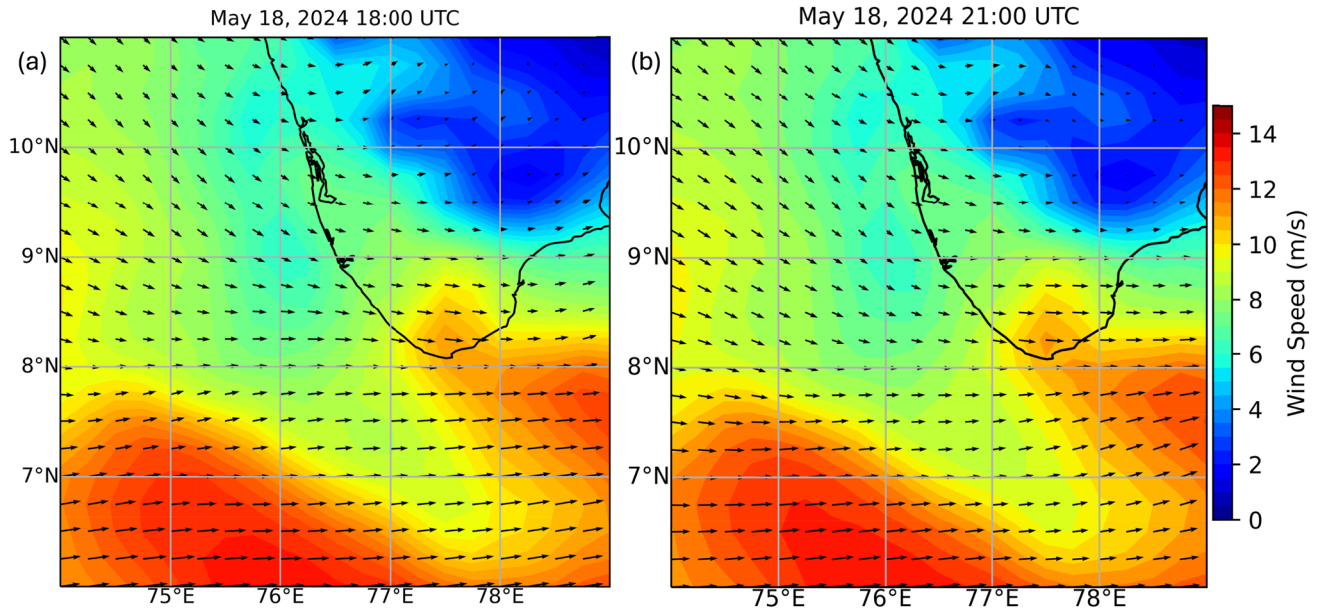

Fig. 13 ERA5 wind speed at 850 hPa on May 18, 2024 **a** at 18:00 UTC. **b** at 21:00 UTC. The colour in background represents the magnitude of the wind speed

Summary and Conclusion

The scatterometers, while providing valuable global wind field observations, face significant data contamination issues during isolated rain events. This present study assesses the impact of rain on newly launched Ku-band OSCAT-3 scatterometer wind measurements. The study utilizes one month of observations from May 2024 over ISMR. The statistical analysis reveals of rain impact on OSCAT-3 winds shows positive bias at low to moderate wind speeds due to enhanced backscatter caused by rain. With increasing rain intensity, the correlation coefficient between OSCAT-3 and ECMWF-ERA5 wind speed and direction decrease and RMSE (mean bias) increases. This indicates that the scatterometer winds are degraded in the presence of rain. The study also discusses a case study of the pre-monsoon heavy rainfall on 18 May 2024 over the southern peninsula. The synoptic analysis shows significant potential of convection in the region with low OLR (<150 w/m^2) values and high CAPE (~ 3751 J/kg). The wind fields from both DWR and OSCAT-3 demonstrate substantial convergence near the coast which may be due to the localised uplifting mechanism responsible for the development of the organized precipitation bands. The combined use of OSCAT-3 and DWR enhances the wind field analysis especially over the coastal areas.

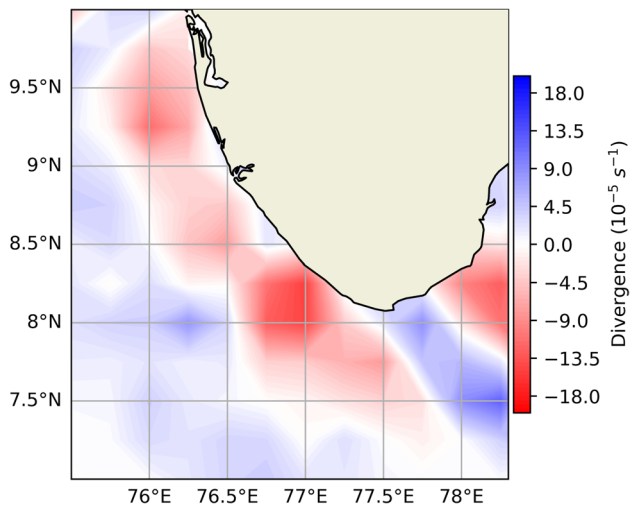

Fig. 14 The divergence of daily analysed L4 OSCAT-3 winds on May 18, 2024

The study highlights the importance of considering the impact of rain contamination on scatterometer winds. The approach of combining wind data from DWR and scatterometer can substantially enhance our understanding of atmospheric phenomena and give a wind field at very high spatial and temporal resolution for both scientific research and operational prediction. The synergy improves the early warning ability, model performance and decision-making.

Acknowledgements The authors thank the financial support under Oceansat-3 Utilization Programme by Space Application Centre, (SAC), ISRO. One of the authors (SD) thankfully acknowledge financial support under MoES NARM Program (MoES/16/04/2021-RDESS/NARM-4). One of the authors (VT) also thankful for the financial

assistance provided by the University Grant Commission (UGC) as Ph.D. fellowship. We extend our sincere gratitude to the Meteorological and Oceanographic Satellite Data Archival Centre (MOSDAC) portal of SAC, ISRO for providing the TERLS DWR, INSAT-3D OLR and EOS-06 daily analysed winds (L4) data. We also acknowledge the Bhoonidhi portal of National Remote Sensing Centre, ISRO for providing the OSCAT-3 L2B. We are also thankful to University of Wyoming for proving the sounding data, NASA's Earthdata portal for GPM-IMERG data and Copernicus Climate Data Store for ERA5 reanalysis winds.

Author Contributions Vaibhav Tyagi: Material preparation, Methodology, Formal analysis, Investigation and Interpretation of results, Writing—original draft and revision. Saurabh Das: Conceptualization, Methodology, Interpretation of results, Supervision, Writing—Review & Editing. Bipasha Paul Shukla: Interpretation of results, Writing—Review & Editing. Abhisek Chakraborty: Interpretation of results, Writing—Review & Editing. Abhishek Chhari: Interpretation of results, Writing—Review & Editing.

Funding The study is supported under the "Oceansat-3 Utilization Programme" by Space Applications Centre, (SAC) ISRO, India.

Data Availability All datasets used in this study are available in the public domain and have been properly cited.

Declarations

Conflict of interest The authors declared that they have no conflict of interest.

References

Belmonte Rivas, M., & Stoffelen, A. (2019). Characterizing ERA-Interim and ERA5 surface wind biases using ASCAT. *Ocean Science, 15*(3), 831–852.

Browning, K. A., & Wexler, R. (1968). The determination of kinematic properties of a wind field using Doppler radar. *Journal of Applied Meteorology and Climatology, 7*(1), 105–113.

Chacko, N., & Jayaram, C. (2024). Assessment of the New Sea Surface Wind Products from EOS-6 Scatterometer. *Journal of the Indian Society of Remote Sensing*, 1–10.

Chakraborty, A., Shukla, B. P., Deb, S. K., & Gairola, R. M. (2022). Paradigm of surface wind fields generated using Scatsat-1 and low-level adjusted INSAT-3D winds during tropical cyclone Amphan. *Remote Sensing Letters, 13*(1), 44–54. https://doi.org/10.1080/2150704X.2021.1985738

Chen, Q., Fan, J., Hagos, S., Gustafson, W. I., Jr., & Berg, L. K. (2015). Roles of wind shear at different vertical levels: Cloud system organization and properties. *Journal of Geophysical Research: Atmospheres, 120*(13), 6551–6574. https://doi.org/10.1002/2015JD023253

CTB-EOS-06. (2023). An ocean of opportunities, Space Applications Centre, ISRO Available at https://www.sac.gov.in/data/Publication/2642/EOS-06%20(Oceansat-3)_Coffee_Table_Book_2023.pdf

Draper, D. W., & Long, D. G. (2004). Evaluating the effect of rain on SeaWinds scatterometer measurements. *Journal of Geophysical Research: Oceans*. https://doi.org/10.1029/2002JC001741

Fu, R., Del Genio, A. D., & Rossow, W. B. (1990). Behavior of deep convective clouds in the tropical Pacific deduced from ISCCP radiances. *Journal of Climate, 3*(10), 1129–1152.

Gabella, M., & Notarpietro, R. (2002). Ground clutter characterization and elimination in mountainous terrain. In Proceedings of ERAD (Vol. 305, No. 311). Available at https://www.copernicus.org/erad/online/erad-305.pdf

Gohil, B. S., Sikhakolli, R., Gangwar, R. K., & Kumar, A. S. K. (2015). Oceanic rain flagging using radar backscatter and noise measurements from Oceansat-2 scatterometer. *IEEE Transactions on Geoscience and Remote Sensing, 54*(4), 2050–2055. https://doi.org/10.1109/TGRS.2015.2494866

Gopalan, K., Sikhakolli, R., & Chakraborty, A. (2019). A Bayesian estimation technique for improving the accuracy of SCATSAT-1 winds in rainy conditions. *IEEE Journal of Selected Topics in Applied Earth Observations and Remote Sensing, 12*(5), 1362–1368. https://doi.org/10.1109/JSTARS.2019.2904088

Hilburn, K. A., Wentz, F. J., Smith, D. K., & Ashcroft, P. D. (2006). Correcting active scatterometer data for the effects of rain using passive radiometer data. *Journal of Applied Meteorology and Climatology, 45*(3), 382–398. https://doi.org/10.1175/JAM2357.1

Huddleston, J. N., & B. W. Stiles. (2000a). Correcting active scatterometer data for the effects of rain using passive microwave data. JPL Product Description version 2.1, https://doi.org/10.1175/JAM2357.1

Huddleston, J. N., & B. W. Stiles. (2000b). A multi-dimensional histogram rain flagging technique for SeaWinds on QuikSCAT. In *Proceedings of the International Geoscience and Remote Sensing Symposium*. IGARSS 2000, Vol. 3, Honolulu, HI, IEEE, 1232–1234. https://doi.org/10.1109/IGARSS.2000.858077

Huffman, G. J., Bolvin, D. T., Braithwaite, D., Hsu, K., Joyce, R., Xie, P., & Yoo, S. H. (2015). NASA global precipitation measurement (GPM) integrated multi-satellite retrievals for GPM (IMERG). Algorithm theoretical basis document (ATBD) version, 4(26), 30. Available at https://gpm.nasa.gov/sites/default/files/2020-05/IMERG_ATBD_V06.3.pdf

IMD-Press Release, 18 May, 2024. Heavy to very heavy rainfall very likely to continue over south Peninsular India till 23rd withextremely heavy falls during 19–21 May, 2024. Available at https://internal.imd.gov.in/press_release/20240518_pr_3005.pdf

Lhermitte, R. M. (1961). Precipitation motion by pulse Doppler. In *Proceeding of the 9th Weather Radar Conference, organized by the American Meteorological Society (AMS)*, pp. 218–223.

Li, N., Wei, M., Mu, X., & Zhao, C. (2015). A support vector machine-based VVP wind retrieval method. *Atmospheric Science Letters, 16*(3), 331–337. https://doi.org/10.1002/asl2.564

Mishra, S., Shanmuga Sundari, J., Channabasava, B., & Anandan, V. K. (2020). First indigenously developed polarimetric C-band Doppler weather radar in India and its first hand validation results. *Journal of Electromagnetic Waves and Applications, 34*(6), 825–840. https://doi.org/10.1080/09205071.2020.1742798

Nonaka, K., Nishimura, S., & Igarashi, Y. (2019). Utilization of estimated sea surface wind data based on Himawari-8/9 low-level AMVs for tropical cyclone analysis. RSMC Tokyo Typhoon Center Technical Review, 21. Available at https://www.jma.go.jp/jma/jma-eng/jma-center/rsmc-hp-pub-eg/techrev/text21-3.pdf

Owen, M. P., & Long, D. G. (2009). Land-contamination compensation for QuikSCAT near-coastal wind retrieval. *IEEE Transactions on Geoscience and Remote Sensing, 47*(3), 839–850. https://doi.org/10.1109/TGRS.2008.2005633

Panda, S. (2019). Quality control and Post-processing of ISRO Doppler Weather Radars. https://doi.org/10.13140/RG.2.2.14909.49127

Pastushkov, R. S. (1975). The effects of vertical wind shear on the evolution of convective clouds. *Quarterly Journal of the Royal Meteorological Society, 101*(428), 281–291. https://doi.org/10.1002/qj.49710142811

Priftis, G., Lang, T. J., & Chronis, T. (2018). Combining ASCAT and NEXRAD retrieval analysis to explore wind features of mesoscale oceanic systems. *Journal of Geophysical Research: Atmospheres, 123*(18), 10–341. https://doi.org/10.1029/2017JD028137

Saikrishna, T. S., Ramu, D. A., & Osuri, K. K. (2021). Inter-comparison of high-resolution satellite precipitation products over India during the summer monsoon season. *Meteorology and Atmospheric Physics, 133*, 1675–1690. https://doi.org/10.1007/s00703-021-00829-7

Sarkar, A. (2003). Space based techniques for remote sensing of oceanic winds: A review. Mausam, 54(1), 111–120. https://doi.org/10.54302/mausam.v54i1.1496

Singh, S., Tiwari, R. K., Sood, V., Kaur, R., & Prashar, S. (2022). The Legacy of Scatterometers: Review of applications and perspective. *IEEE Geoscience and Remote Sensing Magazine, 10*(2), 39–65. https://doi.org/10.1109/MGRS.2022.3145500

Stiles, B. W., & Dunbar, R. S. (2010). A neural network technique for improving the accuracy of scatterometer winds in rainy conditions. IEEE Transactions on Geoscience and Remote Sensing, 48(8), 3114–3122. https://ieeexplore.ieee.org/abstract/document/5475188/

Stiles, B. W., & Yueh, S. H. (2002). Impact of rain on spaceborne Ku-band wind scatterometer data. *IEEE Transactions on Geoscience and Remote Sensing, 40*(9), 1973–1983.

Subrahmanyam, K. V., & Kumar, K. K. (2022). C-band polarimetric Doppler Weather Radar observations during an extreme precipitation event and associated dynamics over Peninsular India. *Natural Hazards, 114*(2), 1307–1322. https://doi.org/10.1007/s11069-022-05426-4

Tournadre, J., & Quilfen, Y. (2003). Impact of rain cell on scatterometer data: 1. *Theory and modeling. Journal of Geophysical Research: Oceans*. https://doi.org/10.1029/2002JC001428

Tournadre, J., & Quilfen, Y. (2005). Impact of rain cell on scatterometer data: 2. Correction of Seawinds measured backscatter and wind and rain flagging. *Journal of Geophysical Research: Oceans*. https://doi.org/10.1029/2004JC002766

Vulpiani, G., Montopoli, M., Passeri, L. D., Gioia, A. G., Giordano, P., & Marzano, F. S. (2012). On the use of dual-polarized C-band radar for operational rainfall retrieval in mountainous areas. *Journal of Applied Meteorology and Climatology, 51*(2), 405–425.

Weissman, D. E., & Bourassa, M. A. (2008). Measurements of the effect of rain-induced sea surface roughness on the QuikSCAT scatterometer radar cross section. *IEEE Transactions on Geoscience and Remote Sensing, 46*(10), 2882–2894. https://doi.org/10.1109/TGRS.2008.2001032

Weissman, D. E., Stiles, B. W., Hristova-Veleva, S. M., Long, D. G., Smith, D. K., Hilburn, K. A., & Jones, W. L. (2012). Challenges to satellite sensors of ocean winds: Addressing precipitation effects. *Journal of Atmospheric and Oceanic Technology, 29*(3), 356–374. https://doi.org/10.1175/JTECH-D-11-00054.1

Xavier, A., Manoj, M. G., & Mohankumar, K. (2018). On the dynamics of an extreme rainfall event in northern India in 2013. *Journal of Earth System Science, 127*, 1–13. https://doi.org/10.1007/s12040-018-0931-6

Xu, Q., Liu, S., & Xue, M. (2006). Background error covariance functions for vector wind analyses using Doppler-radar radial-velocity observations. *Quarterly Journal of the Royal Meteorological Society: A Journal of the Atmospheric Sciences, Applied Meteorology and Physical Oceanography, 132*(621C), 2887–2904. https://doi.org/10.1256/qj.05.202

Zhang, C. (1993). Large-scale variability of atmospheric deep convection in relation to sea surface temperature in the tropics. *Journal of Climate, 6*(10), 1898–1913.

Zhang, J. W., & Atkinson, B. W. (1995). Stability and wind shear effects on meso-scale cellular convection. *Boundary-Layer Meteorology, 75*(3), 263–285. https://doi.org/10.1007/BF00712697

Zhang, J., & Wang, S. (2006). An automated 2D multipass Doppler radar velocity dealiasing scheme. *Journal of Atmospheric and Oceanic Technology, 23*(9), 1239–1248. https://doi.org/10.1175/JTECH1910.1

Zhao, X., Lin, W., Portabella, M., Wang, Z., & He, Y. (2022). Effects of rain on CFOSAT scatterometer measurements. *Remote Sensing of Environment, 274*, Article 113015. https://doi.org/10.1016/j.rse.2022.113015

Zhou, X., He, L., He, Z., & Tang, Z. (2019). Multiresolution and velocity vector average processing algorithm for wind field retrieval based on Doppler radar. *Journal of Applied Remote Sensing, 13*(4), 046514–046514. https://doi.org/10.1117/1.JRS.13.046514